

# The SAMI Galaxy Survey: the link between angular momentum and optical morphology

L. Cortese<sup>\*1</sup>, L. M. R. Fogarty<sup>2,3</sup>, K. Bekki<sup>1</sup>, J. van de Sande<sup>2</sup>, W. Couch<sup>4</sup>,  
 B. Catinella<sup>1</sup>, M. Colless<sup>3,5</sup>, D. Obreschkow<sup>1,3</sup>, D. Taranu<sup>1,3</sup>, E. Tescari<sup>3,6</sup>, D. Barat<sup>5</sup>,  
 J. Bland-Hawthorn<sup>2</sup>, J. Bloom<sup>2</sup>, J. J. Bryant<sup>2,3,4</sup>, M. Cluver<sup>7</sup>, S. M. Croom<sup>2,3</sup>,  
 M. J. Drinkwater<sup>3,8</sup>, F. d’Eugenio<sup>5</sup>, I. S. Konstantopoulos<sup>4,9</sup>, A. Lopez-Sanchez<sup>4,10</sup>,  
 S. Mahajan<sup>11</sup>, N. Scott<sup>2,3</sup>, C. Tonini<sup>6</sup>, O. I. Wong<sup>1</sup>, J. T. Allen<sup>2,3</sup>, S. Brough<sup>3,4</sup>,  
 M. Goodwin<sup>4</sup>, A. W. Green<sup>4</sup>, I.-T. Ho<sup>5,12</sup>, L. S. Kelvin<sup>13</sup>, J. S. Lawrence<sup>4</sup>,  
 N. P. F. Lorente<sup>4</sup>, A. M. Medling<sup>5</sup>, M. S. Owers<sup>4,10</sup>, S. Richards<sup>2,3,4</sup>, R. Sharp<sup>3,5</sup>,  
 S. M. Sweet<sup>5</sup>

<sup>1</sup>International Centre for Radio Astronomy Research, The University of Western Australia, 35 Stirling Highway, Crawley WA 6009, Australia

<sup>2</sup>Sydney Institute for Astronomy, School of Physics, The University of Sydney, Sydney NSW 2006, Australia

<sup>3</sup>ARC Centre of Excellence for All-Sky Astrophysics (CAASTRO)

<sup>4</sup>Australian Astronomical Observatory, PO Box 915, North Ryde NSW 1670, Australia

<sup>5</sup>Research School of Astronomy and Astrophysics, Australian National University, Canberra ACT 2611, Australia

<sup>6</sup>School of Physics, the University of Melbourne, Parkville, VIC 3010, Australia

<sup>7</sup>Department of Physics and Astronomy, University of the Western Cape, Robert Sobukwe Road, Bellville, 7535, South Africa

<sup>8</sup>School of Mathematics and Physics, University of Queensland, QLD 4072, Australia

<sup>9</sup>Envizi Group Suite 213, National Innovation Centre, Australian Technology Park, 4 Cornwallis Street, Eveleigh NSW 2015, Australia

<sup>10</sup>Department of Physics and Astronomy, Macquarie University, NSW 2109, Australia

<sup>11</sup>Indian Institute of Science Education and Research Mohali-IISERM, Knowledge City, Sector 81, Manauli, P.O. 140306, India

<sup>12</sup>Institute for Astronomy, University of Hawaii, 2680 Woodlawn Drive, Honolulu, HI 96822, USA

<sup>13</sup>Astrophysics Research Institute, Liverpool John Moores University, IC2, Liverpool Science Park, 146 Brownlow Hill, Liverpool, L3 5RF, UK

## ABSTRACT

We investigate the relationship between stellar and gas specific angular momentum  $j$ , stellar mass  $M_*$  and optical morphology for a sample of 488 galaxies extracted from the SAMI Galaxy Survey. We find that  $j$ , measured within one effective radius, monotonically increases with  $M_*$  and that, for  $M_* > 10^{9.5} M_\odot$ , the scatter in this relation strongly correlates with optical morphology (i.e., visual classification and Sérsic index). These findings confirm that massive galaxies of all types lie on a plane relating mass, angular momentum and stellar light distribution, and suggest that the large-scale morphology of a galaxy is regulated by its mass and dynamical state. We show that the significant scatter in the  $M_* - j$  relation is accounted for by the fact that, at fixed stellar mass, the contribution of ordered motions to the dynamical support of galaxies varies by at least a factor of three. Indeed, the stellar spin parameter (quantified via  $\lambda_R$ ) correlates strongly with Sérsic and concentration indices. This correlation is particularly strong once slow-rotators are removed from the sample, showing that late-type galaxies and early-type fast rotators form a continuous class of objects in terms of their kinematic properties.

**Key words:** galaxies:evolution–galaxies: fundamental parameters–galaxies: kinematics and dynamics

## 1 INTRODUCTION

Since the dawn of extragalactic astronomy, it has been clear that galaxies show an impressive variety of shapes and sizes.

\* luca.cortese@uwa.edu.au

Despite this diversity, astronomers soon realised that galaxies can be grouped into distinct families according to their visual appearance (e.g., [Herschel 1786](#); [Rosse 1850](#)). Particularly successful have been the classification schemes proposed by [Reynolds \(1920\)](#) and [Hubble \(1926\)](#), now generally known as the Hubble sequence (see also [de Vaucouleurs 1959](#); [van den Bergh 1976](#)). After nearly a century, the Hubble sequence is still a crucial element in our theoretical framework of galaxy formation and evolution, and understanding its origin remains a challenge for current astronomical research.

Before the advent of charge-coupled devices (CCDs), galaxies were almost always classified via visual inspection following the Hubble classification ([Nilson 1973](#); [de Vaucouleurs et al. 1991](#)). The high quality of photographic plates, combined with the proximity of the galaxies studied, allowed astronomers to notice tiny details in the morphology of galaxies and discriminate between various subclasses in the Hubble sequence. Indeed, some of the most accurate morphological classifications to date (e.g., [Binggeli et al. 1985](#)) are still based on analysis performed on photographic plates.

The situation changed completely with the era of CCD-based, large-area surveys. Firstly, as the average distances of the galaxies studied has increased remarkably, the fine details (e.g., dust lanes, prominence of spiral arms, faded disks) needed to perform accurate visual classifications are less obvious. Secondly, with the number of galaxies imaged increasing from a few thousands to millions, by-eye classification has become inefficient without the help of citizen science ([Lintott et al. 2008](#)). Thirdly, and perhaps most importantly, the Hubble scheme turned out not to be ideal for a quantitative comparison with theoretical models, as it is challenging to apply the same selection criteria used for observations to simulated data.

Thus, in the last few decades, we have seen the emergence of a plethora of new ‘morphological indicators’ based on the stellar distribution (e.g., [Abraham et al. 1994](#); [Ber-shady et al. 2000](#); [Goto et al. 2003](#); [Lotz et al. 2004](#)), optical colour of galaxies (e.g., [Strateva et al. 2001](#); [Chilingarian & Zolotukhin 2012](#)), or combinations of the two (e.g., [Conselice 1999](#); [Banerji et al. 2010](#); [Vulcani et al. 2014](#)), aimed at providing a more modern view of the Hubble sequence and an easier comparison with numerical simulations. These morphological indicators are now common practice, and have generally replaced visual classification as a tool for dividing galaxies into different families. However, despite their success and applicability to large samples of galaxies, such techniques sometimes fail to discriminate between different classes of objects. Particularly challenging is the regime of massive, bulge-dominated, optically-red galaxies where structural parameters and colours alone cannot always distinguish between rotationally- and dispersion-supported systems ([Scodreggio et al. 2002](#); [Emsellem et al. 2007, 2011](#)), or between quiescent and star-forming galaxies ([Cortese 2012](#)). The main issue is that all of the above classification schemes, even when combined, are incomplete and are missing information about some crucial physical properties of galaxies such as their kinematics or star formation activity.

In particular, it has been clear for decades that information on the stellar and gas kinematics can provide us with a more physically-motivated morphological classifica-

tion (e.g., [Fall 1983](#); [Kormendy 1993](#); [Kormendy & Kennicutt 2004](#); [Snyder et al. 2015](#); [Teklu et al. 2015](#)). After all, the common assumption beyond the bulge vs. disk bimodality is that bulges are mostly supported by random motions, whereas disks are primarily supported by rotation. However, until very recently, the lack of resolved spectroscopic surveys for large, representative samples of galaxies has limited our ability to quantify the link between galaxy kinematics and morphology.

Thanks to significant technical improvements, integral field spectroscopic (IFS) surveys of thousands of galaxies are now a reality. Pioneers in this new field have been the Spectrographic Areal Unit for Research on Optical Nebulae (SAURON, [Bacon et al. 2001](#)) and ATLAS<sup>3D</sup> ([Cappellari et al. 2011a](#)) surveys. By taking advantage of resolved stellar kinematics out to one effective radius ( $r_e$ ), these projects have shown that the kinematic properties of early-type galaxies are not strongly correlated with their stellar light distribution ([Krajinović et al. 2013](#)). They thus proposed a new classification scheme where early-types are divided into fast and slow rotators depending on the value of their spin ([Emsellem et al. 2011](#)), quantified via the  $\lambda_R$  parameter ([Emsellem et al. 2007](#)). Interestingly, it is still a matter of debate whether or not these conclusions hold once  $\lambda_R$  is measured including the outer parts of galaxies ([Foster et al. 2013](#); [Arnold et al. 2014](#)).

Two complementary approaches would naturally extend on existing kinematic studies. First, deeper, spatially resolved spectroscopy reaching larger galactic radii is needed to capture most of the angular momentum. Second, a uniform kinematic analysis of galaxies of all Hubble types is required to build a unified picture of the role of kinematics in galaxy evolution. Progress in both directions has been made by [Romanowsky & Fall \(2012, hereafter RF12\)](#) using a combination of stellar and gas kinematic measurements from the literature. They investigated the stellar mass ( $M_*$ ) vs. specific angular momentum ( $j$ , the angular momentum per unit of mass) relation to quantify the connection between  $j$  and morphology. Following the original work of [Fall \(1983\)](#), they showed that the scatter in the  $M_*$ - $j$  relation correlates with morphology (i.e., visual classification or bulge-to-total ratio) across the entire Hubble sequence. This suggests that, also among early-type galaxies, optical morphology statistically correlates with kinematics. Unfortunately, a comparison between RF12 and ATLAS<sup>3D</sup> is not straightforward. Not only did RF12 mainly take advantage of long-slit spectroscopy and not 2D resolved maps, but they also measured the total angular momentum of galaxies while the ATLAS<sup>3D</sup> work is based on the spin parameter estimated within the inner one effective radius.

For late-type galaxies, [Obreschkow & Glazebrook \(2014, hereafter OG14\)](#) recently improved on this limitation by taking advantage of resolved HI velocity maps for 16 late-type galaxies from the The HI Nearby Galaxy Survey (THINGS, [Walter et al. 2008](#)). They revealed an even tighter relation between  $M_*$ ,  $j$  and the bulge-to-disk ratio. However, because their sample included only late-type galaxies and  $j$  is integrated across the entire disk, a comparison with ATLAS<sup>3D</sup> results is also impossible.

To make further progress in this field, we need spatially-resolved velocity maps across the whole range of galaxy morphologies. The Sydney-AAO Multi-object Integral field

(SAMI, Croom et al. 2012) Galaxy Survey (Bryant et al. 2015), the first large IFS survey, provides an ideal sample for which such an investigation can be carried out now. Like all current IFS surveys, SAMI does not allow us to trace gas and stellar kinematics up to, or beyond, one optical radius for a statistically large number of objects.

In this paper, we take advantage of SAMI data to extend the works of ATLAS<sup>3D</sup>, RF12 and OG14 by investigating the role played by stellar and gas kinematics, within one effective radius, in shaping galaxy morphology across the entire Hubble sequence. The large number statistics, high-quality two-dimensional velocity maps and the wide range of galaxy properties provided by the SAMI Galaxy Survey not only allow us to ease the tension between previous works, but also provide us with a unique window on the physical link between stellar density distribution, spin and angular momentum.

This paper is organized as follows. In Sec. 2 we describe the SAMI Galaxy Survey sample, the procedure to estimate stellar and gas velocity fields, and the ancillary data used in this paper. In Sec. 3 we investigate the link between central stellar and gas specific angular momentum, stellar mass, and optical morphology. In Sec. 4, we show the role played by the spin parameter, estimated via  $\lambda_R$ , in the scatter of the  $M_*-j_*$  relation. In Sec. 5, we compare our results with the predictions of theoretical models. Finally, the implications of our results are discussed in Sec. 6.

Throughout this paper, we use a flat  $\Lambda$  cold dark matter concordance cosmology:  $H_0 = 70 \text{ km s}^{-1} \text{ Mpc}^{-1}$ ,  $\Omega_0=0.3$ ,  $\Omega_\Lambda=0.7$ .

## 2 THE DATA

The SAMI Galaxy Survey is targeting  $\sim 3400$  galaxies in the redshift range  $0.004 < z < 0.095$  with the SAMI integral field unit, installed at the 3.9m Anglo-Australian Telescope. The main goal of this survey is to provide a complete census of the resolved optical properties of nearby galaxies (e.g., star formation rate, age, metallicity, kinematics) across a wide range of environments (Bryant et al. 2015).

SAMI takes advantage of photonic imaging bundles (‘hexabundles’, Bland-Hawthorn et al. 2011; Bryant et al. 2014) to simultaneously observe 12 galaxies across a 1 degree field of view. Each hexabundle is composed of 61 optical fibres, each with a diameter of  $\sim 1.6''$ , covering a total circular field of view of  $\sim 14.7''$  in diameter. SAMI fibres are fed into the AAOmega dual-beam spectrograph (Sharp et al. 2006), providing coverage of the 3700-5700 Å and 6300-7400 Å wavelength ranges at resolutions  $R \sim 1730$  and  $R \sim 4500$ , respectively. These correspond to a velocity full-width at half-maximum of  $\sim 170 \text{ km s}^{-1}$  in the blue, and  $\sim 65 \text{ km s}^{-1}$  in the red.

In this paper, we focus on a subsample of the 824 galaxies from the last SAMI internal data release (v0.9 - October 2015) in the footprint of the Galaxy And Mass Assembly survey (GAMA, Driver et al. 2011) for the wealth of multiwavelength data available. SAMI pointings targeting specific clusters outside the GAMA footprint (see Bryant et al. 2015 and Owers et al. in prep.) are not included. A detailed description of the data reduction technique is presented in Sharp et al. (2015) and Allen et al. (2015a). As described in

Bryant et al. (2015), the configuration of each SAMI plate is done to maximize the number of objects observable within a SAMI field of view, and no pre-selection on morphology or environment is introduced during the tiling process.

### 2.1 Stellar and ionised gas kinematics

Stellar and ionized gas line-of-sight velocity and velocity dispersion two-dimensional maps were obtained from the re-sampled SAMI cubes ( $0.5'' \times 0.5''$  spaxel size) as follows.

Stellar line-of-sight velocity and intrinsic dispersion maps were extracted from the SAMI cubes by using the penalised pixel-fitting routine pPXF, developed by Cappellari & Emsellem (2004). We fitted the blue and red channels simultaneously, after having convolved the red spectra to the same (i.e., lower) resolution of the blue cube and interpolated on to a grid with the same wavelength spacing.

We used annular binned spectra (which follow the optical ellipticity and position angle of the target) with signal-to-noise  $\geq 25$  for deriving optimal templates as opposed to obtaining an optimal template for each individual spaxel. Indeed, individual spaxels usually do not meet the signal-to-noise required to extract a reliable optimal template. For each annulus, we determined the best combination of the 985 stellar template spectra from the MILES stellar library (Sánchez-Blázquez et al. 2006) that is able to reproduce the galaxy spectrum. This best fit template is then used to fit every spaxel within that annulus having a signal-to-noise per spectral pixel greater than 3. We prefer annular to Voronoi bins because they allow us to follow more closely any radial gradients in the properties of stellar populations. An extensive description of the SAMI stellar kinematics products will be presented in an upcoming paper (van de Sande et al., in prep.).

While the choice of optimal template is important for a reliable estimate of velocity dispersion, it has no significant effect on the line-of-sight velocity field, i.e., the critical parameter for the estimate of specific angular momentum. Indeed, we find the same results even if optimal templates calibrated for just a central  $2''$  aperture are used to fit the entire SAMI field-of-view, as described in Fogarty et al. (2014) and Cortese et al. (2014). Moreover, Fogarty et al. (2015) and van de Sande et al. (in prep.) have shown that, for the range of stellar velocity dispersions typical of the galaxies investigated in this work ( $\sigma \geq 50 \text{ km s}^{-1}$ ), our technique is able to recover both dispersion and line-of-sight velocities, with no significant systematic bias.

Gas velocity maps were obtained using the new LZIFU IDL fitting routine (Ho et al. 2016b; see also Ho et al. 2014). After subtracting the stellar continuum with pPXF, LZIFU fits up to 11 strong optical emission lines ([OII] $\lambda\lambda 3726, 29$ , H $\beta$ , [OIII] $\lambda\lambda 4959, 5007$ , [OI] $\lambda 6300$ , [NII] $\lambda\lambda 6548, 83$ , H $\alpha$ , and [SII] $\lambda\lambda 6716, 31$ ) as a simple Gaussian simultaneously using MPFIT (Markwardt 2009), constraining all the lines to share the same velocity and dispersion. We use the reconstructed kinematic maps to measure gas rotation and intrinsic velocity dispersion.

Examples of SAMI stellar and gas velocity fields are presented in Allen et al. (2015a, Fig. 3,4), Allen et al. (2015b, Fig. 3,8), Cecil et al. (2015, Fig. 6) and Ho et al. (2016a, Fig. 7,A1).

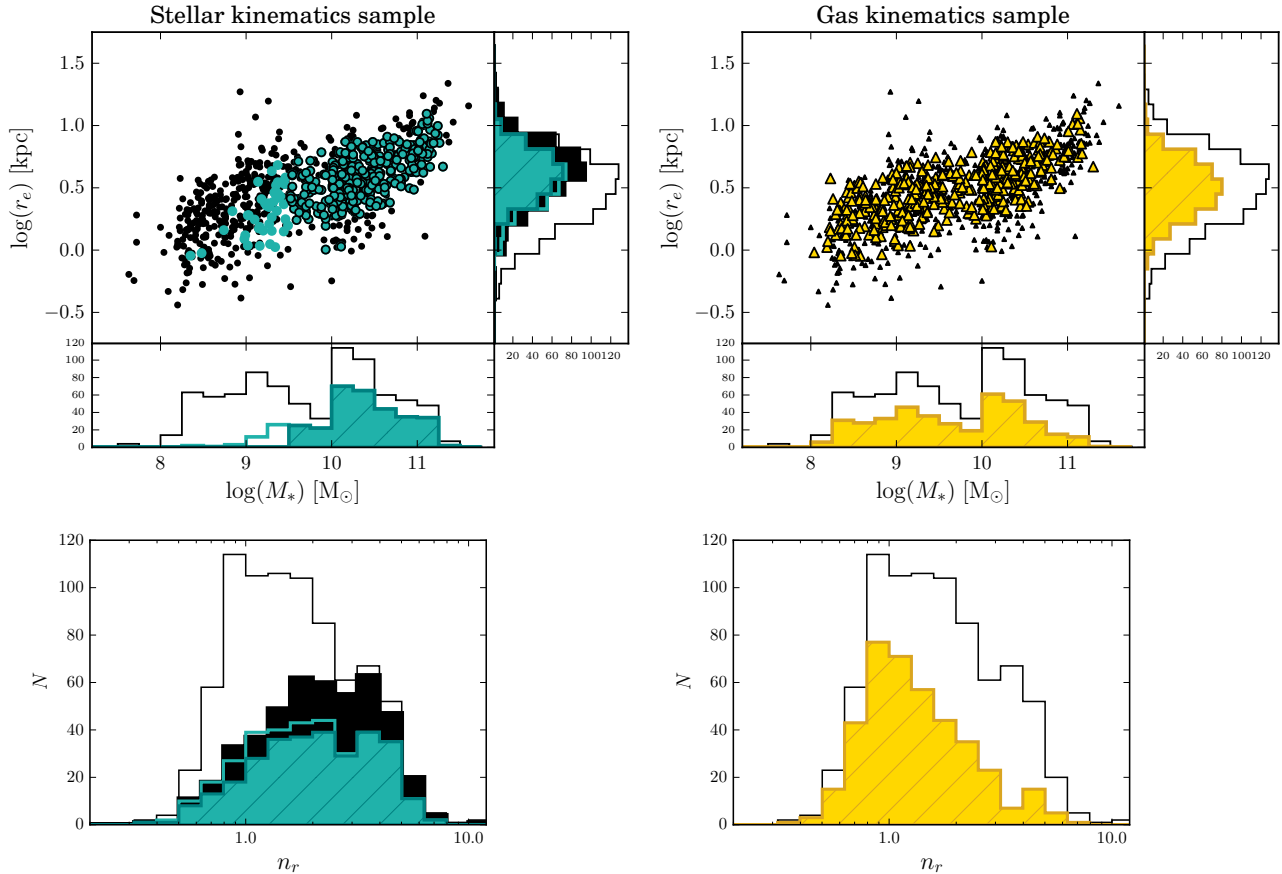


**Figure 1.** *Left panels:* The  $M_*$ - $r_e$  relation,  $M_*$  and  $r_e$  distributions (top), and Sérsic index distribution (bottom) for galaxies with stellar kinematics in our sample. The black points and empty histograms show our parent sample of 824 galaxies. Teal points and teal empty histograms are galaxies with reliable stellar kinematics as defined in Sec. 2.1; black-circled teal points and teal filled histogram show our final sample after imposing a cut at  $M_* = 10^{9.5} M_\odot$ . The black filled histogram shows the distribution for galaxies in our parent sample with  $M_* > 10^{9.5} M_\odot$ . *Right panels:* Same as left for the sample with reliable gas kinematics. Note that no cut in  $M_*$  has been applied.

## 2.2 Ancillary data

The SAMI data have been combined with multiwavelength observations obtained as part of the GAMA survey. Stellar masses ( $M_*$ ) are estimated from  $g - i$  colours and  $i$ -band magnitudes following Taylor et al. (2011), as described in Bryant et al. (2015), assuming a Chabrier (2003) initial mass function and continuous, exponentially declining, star formation histories. The typical random uncertainty on stellar masses is  $\sim 0.1$  dex. Effective radii, position angles and ellipticities are taken from the 2D one-component Sérsic fits to the Sloan Digital Sky Survey (York et al. 2000)  $r$ -band images presented in Kelvin et al. (2012). As shown by Lange et al. (2015), this dataset provides a good benchmark for the size distribution of local galaxies, and the radii estimated from Sérsic fits represent an improvement on earlier estimates based on circular apertures.

In order to investigate the link between stellar and gas kinematics and morphology, we use one parametric and one non parametric indicator, the Sérsic index measured in  $r$ -band ( $n_r$ , Kelvin et al. 2012) and concentration index (defined as the ratio of the SDSS Petrosian radii containing 90% and 50% of the total  $r$ -band luminosity  $R_{90}/R_{50}$ ), respectively. We use the SDSS Petrosian radii instead of those

obtained from the one-component Sérsic fit in order to have two independent morphological indicators. Indeed, by construction, the concentration index can be estimated analytically from the Sérsic index if the radii are derived from the one-component Sérsic fits.

We also perform a visual morphological classification taking advantage of the SDSS DR9 (Ahn et al. 2012) colour images. At least eight of us independently classified each galaxy following the scheme used by Kelvin et al. (2014). First, galaxies are divided into late- and early-types according to their morphology, presence of spiral arms and/or signs of star formation. Then, early-types with just a bulge are classified as ellipticals (E) and early-types with disks as S0s. Similarly, late-type galaxies with only a disk component are Sc or later, while disk plus bulge late types are Sa-Sb. All votes are then combined and, for each galaxy, the type with at least 66% of the votes is chosen. If no agreement is found, we combine adjacent votes into intermediate classes (E/S0, S0/Sa,Sbc) and, if the 66% threshold is met, the galaxy is given the corresponding intermediate type. For those few cases (less than 5% of our sample) for which even this second step fails, a new round of classifications is performed. However, this time the choice is limited to the two types most voted during the first iteration, and the galaxy is marked

as unclassified if no agreement is reached. Just eight objects in our sample with either reliable gas or stellar kinematics were unclassified under this scheme. These galaxies will not appear in those plots in which objects are colour-coded by morphological type.

### 2.3 Sample selection

To obtain homogeneous and reliable estimates of the specific angular momentum within one effective radius, we first restrict our sample to those galaxies with an  $r$ -band effective diameter smaller than  $15''$  (the size of a SAMI bundle), and greater than  $4''$  to make sure that our targets are resolved. Then, following Cortese et al. (2014), we discard all galaxies for which more than 20% of the spaxels have an uncertainty greater than  $20 \text{ km s}^{-1}$  and  $50 \text{ km s}^{-1}$  in the line-of-sight velocity of gas and stars, respectively. This additional cut ensures that we restrict our analysis to those galaxies for which the gas and stellar kinematic properties are reliable. Finally, we visually inspect each velocity map and remove problematic cases (e.g., contamination by foreground/background objects, disturbed systems for which the photometric ellipticity and/or position angles are highly inconsistent with the orientation of velocity field, etc.;  $\sim 10\%$  of the remaining sample). After all these cuts, we are left with 397 and 341 galaxies with reliable gas and stellar kinematics, respectively.

To investigate the parameter space covered by galaxies with reliable 2D stellar or gas kinematics, in Fig. 1 we compare their  $M_*$ - $r_e$  relation and Sérsic index distribution (teal), with those of our parent sample of 824 galaxies (black). As clearly shown in the left panels of Fig. 1, for  $M_* < 10^{9.5} M_\odot$  we do not recover the stellar kinematics for the entire range of sizes covered by our sample and preferentially lose systems with large radii. This selection bias roughly corresponds to a surface brightness limit at  $1 r_e$  of  $\sim 23 \text{ mag arcsec}^2$  in  $r$ -band. Below this, our continuum signal-to-noise is too low to obtain reliable stellar kinematics. For this reason, we decided to limit our investigation of the stellar angular momentum to galaxies more massive than  $10^{9.5} M_\odot$  (297 galaxies), where size and Sérsic index distributions for our final sample (filled teal histogram) are representative of the parent sample (filled black histogram).

Conversely, galaxies with reliable gas kinematics (yellow points and histograms in the right panel of Fig. 1) cover the same range of sizes and masses of our parent sample, although they clearly under-sample spheroid-dominated systems as highlighted by their Sérsic index distribution (golden histogram in Fig. 1). We will further discuss this bias in Sec. 3.2.

In summary, our final sample is composed of 488 galaxies: 397 and 297 galaxies with reliable gas and stellar kinematics, respectively (of which 206 galaxies have both stellar and gas kinematics). It is clear that, while our samples of stellar and gas kinematic measurements are representative of the population of galaxies more massive than  $10^{9.5} M_\odot$  and disk-dominated systems above  $10^8 M_\odot$ , respectively, they are by no means complete. Although this does not significantly bias our investigation of the main driver for scatter in the  $M_*$ - $j$  relation, it could affect the value of the slope of the relation (see also Hyde & Bernardi 2009). Thus, as we will discuss later in the text, a grain of salt must be used in the

interpretation of the slopes of the  $M_*$ - $j$  relations obtained as part of this work.

### 3 THE SPECIFIC ANGULAR MOMENTUM

In theory, following Emsellem et al. (2007), the specific angular momentum of disks can be estimated from 2D resolved line-of-sight velocity maps as:

$$\frac{J}{M} = \frac{\sum_{k=1}^n M_k R_k |V_k|}{\sum_{k=1}^n M_k} \quad (1)$$

where  $M_k$  is the total mass included in spaxel  $k$ ,  $R_k$  is its distance from the galaxy center in the plane of the disk (i.e., the de-projected radius), and  $V_k$  is its rotational velocity. In practice, SAMI data do not provide us with a distribution of total mass, rotational velocity and de-projected radius, but only with stellar light distribution and projected line-of-sight velocity and radius. Thus, a few approximations to Eq. 1 are needed in order to estimate a proxy for the specific angular momentum from SAMI data.

Firstly, assuming that the optical ellipticity is a good proxy for the galaxy inclination, the de-projected radius at each spaxel can be easily computed knowing the axis ratio and position angle of the galaxy.

Secondly, the spectral coverage of SAMI data does not allow us to construct 2D colour maps in the SDSS filters and use them to estimate the typical mass-to-light ratio in each spaxel (e.g., following standard recipes as in Bell et al. 2003; Zibetti et al. 2009; Taylor et al. 2011). Thus, we simply substitute  $M_k$  in Eq. 1 with the average continuum flux across the entire wavelength range covered by SAMI,  $F_k$ . We further discuss the implications of this assumption in the next section, showing that it does not affect the main conclusions of this work.

Thirdly, as IFS data provide information on the line-of-sight velocities, we need to correct for inclination in order to recover the rotational velocity of our system. We do so by assuming that, in each spaxel, the rotational velocity is given by:

$$V_k = \frac{V_{k \text{ los}}}{\sin(i)\cos(\theta_k)} \quad (2)$$

where  $V_{k \text{ los}}$  is the line-of-sight velocity,  $\theta_k$  is the azimuthal angle in the galaxy coordinate frame (with zero corresponding to the direction perpendicular to the line of sight) and  $i$  is the galaxy inclination. However, from observations we do not measure  $\theta_k$  directly, but its projection on the plane of the sky  $\phi_k$ . Assuming a thin inclined disk with semi-major axis along the  $x$  direction:

$$\tan(\phi_k) = \frac{y_k}{x_k} = \frac{b}{a} \tan(\theta_k) \quad (3)$$

where  $x_k$  and  $y_k$  are the  $x$  and  $y$  coordinates of spaxel  $k$  with respect to the galaxy center, and  $b$  and  $a$  are the minor

and major axes, respectively. Thus <sup>1</sup>,

$$\tan(\theta_k) = \frac{a}{b} \frac{y_k}{x_k} \quad (4)$$

Finally, inclinations are determined from the  $r$ -band axis ratio ( $b/a$ ) as:

$$\cos(i) = \sqrt{\frac{(b/a)^2 - q_0^2}{1 - q_0^2}} \quad (5)$$

where  $q_0$  is the intrinsic axial ratio of an edge-on galaxy. The value of  $q_0$  is highly uncertain and it is known to vary with the morphology and dynamical properties of galaxies within the range  $\sim 0.1$ - $0.65$  (e.g., [Giovanelli et al. 1997](#); [Weijmans et al. 2014](#)). Here we use  $q_0=0.2$  for all galaxies with a clear disk component (i.e., including S0s), and  $q_0=0.6$  for visually classified ellipticals. We set the inclination to 90 degrees if  $b/a < q_0$ . Our conclusions are not affected if we adopt a value of  $q_0$  which varies smoothly with morphology. As already noted, our technique is based on the assumption that the optical axis ratio is a good proxy for the galaxy inclination. This is consistent with what has been done in previous works.

We remind the reader that our inclination correction is valid for disks, whereas for pure spheroids it systematically overestimates the effect of projection and thus the intrinsic angular momentum. As correcting velocity fields of pure spheroids for inclination is notoriously challenging even when accurate dynamical modeling can be performed (RF12; [Weijmans et al. 2014](#)), we do not attempt to derive an ad-hoc correction for pure elliptical galaxies. Instead, we perform our analysis on both projected and intrinsic (i.e., de-projected) specific angular momentum to show that our main results are independent of the inclination correction adopted. This is also because fewer than 10% of galaxies in our sample (26 out of 297 objects) are classified as pure ellipticals (i.e., do not show the presence of a disk component). An additional check on the reliability of our correction is presented in Sec. 5, where we compare our measurements with model predictions.

To summarize, we define the projected ( $j_p$ ) and intrinsic angular momentum ( $j$ ) as:

$$j_p = \frac{\sum_{k=1}^n F_k R_k |V_{k \text{ los}}|}{\sum_{k=1}^n F_k} \quad (6)$$

and

$$j = \sum_{k=1}^n \frac{F_k R_k |V_{k \text{ los}}|}{\sin(i) \cos(\theta_k)} \times \frac{1}{\sum_{k=1}^n F_k} \quad (7)$$

respectively, where here  $R_k$  is the semi-major axis of the ellipse having minor-to-major axis ratio  $b/a$  (i.e., the intrinsic galaxy radius), on which spaxel  $k$  lies. The sum is performed including only spaxels within an ellipse of semi-major axis  $R_e$  and axis ratio  $b/a$ . The galaxy centre is defined as

<sup>1</sup> Note that, along the minor axis,  $\cos(\theta_k)$  is zero and our correction diverges. To avoid this we impose that  $\cos(\theta_k)$  cannot be smaller than 0.15. This effectively impacts only those spaxels within  $<1.1$  arcsec from the minor axis of the galaxy: i.e., well within our spatial resolution.

the peak of the continuum emission in the SAMI cube. The main difference between our methodology and the one used by RF12 lies in the use of homogeneous resolved velocity maps for all galaxies instead of being mainly based on long-slit spectroscopy (plus the addition of multi-slit, IFS data and kinematics obtained via planetary nebulae or globular clusters). In our case, we can directly use the velocity information in each spaxel, following the 2D distribution of the velocity field. In addition, the difference in the intrinsic axial ratio and inclination correction imply that our  $j$  are systematically lower for pure disks and higher for ellipticals than those obtained using RF12 technique.

Uncertainties on the specific angular momentum are estimated by propagating the uncertainties on continuum flux and velocity derived by pPXF for each spaxel, taking into account the covariance between individual spaxels as described in [Fogarty et al. \(2014\)](#). The average nominal uncertainty in  $j$  is  $\sim 12\%$ , but this does not include the effect of the inclination correction that likely dominates the final error.

### 3.1 The stellar specific angular momentum within one effective radius

In Fig. 2 we plot the projected and intrinsic stellar specific angular momentum,  $j_{*p}$  (top panels) and  $j_*$  (bottom panels) as a function of  $M_*$  for the 297 galaxies with good stellar kinematics in our sample. Galaxies are colour-coded by visual morphology and  $r$ -band Sérsic index in the left and right panels, respectively. It is clear that, for the entire population, the specific angular momentum increases with stellar mass, and that the scatter in both relations correlates with galaxy morphology. The scatter in the average perpendicular distance from the best-fitting bisector linear relation is  $\sim 0.27$  and  $\sim 0.21$  dex for the projected and intrinsic case, respectively<sup>2</sup>.

At fixed stellar mass, disk-dominated systems have higher specific angular momentum than bulge-dominated galaxies. This is even clearer in Fig. 3, where we present the best fits to the  $M_*$ - $j_*$  relation for the four morphological types considered here. The best-fitting parameters are presented in Table 1. All four classes follow roughly parallel relations, with typical offsets of the order of 0.2-0.4 dex in  $j_*$ . Although the scatter in the relation is visibly reduced by the inclination correction, the effect of morphology in driving the spread of the intrinsic versions of the  $M_*$ - $j_*$  relation is still significant. This suggests that our findings are not an inclination effect due to the fact that, statistically, late-type galaxies are flatter than early-types. The only strong difference between the projected and intrinsic relations is the case of elliptical galaxies, which are brought closer to the relation of early-type disks once we correct for inclination. This is due to our conservative approach of assuming a disk geometry also for elliptical galaxies, thus likely overestimating the effect of projection.

In addition to inclination, it is important to investigate whether the differences shown in Fig. 2 and 3 between

<sup>2</sup> All fits in this paper are performed by minimizing the orthogonal scatter while taking into account uncertainties on each variable using the hyperfit code developed by [Robotham & Obreschkow \(2015\)](#).

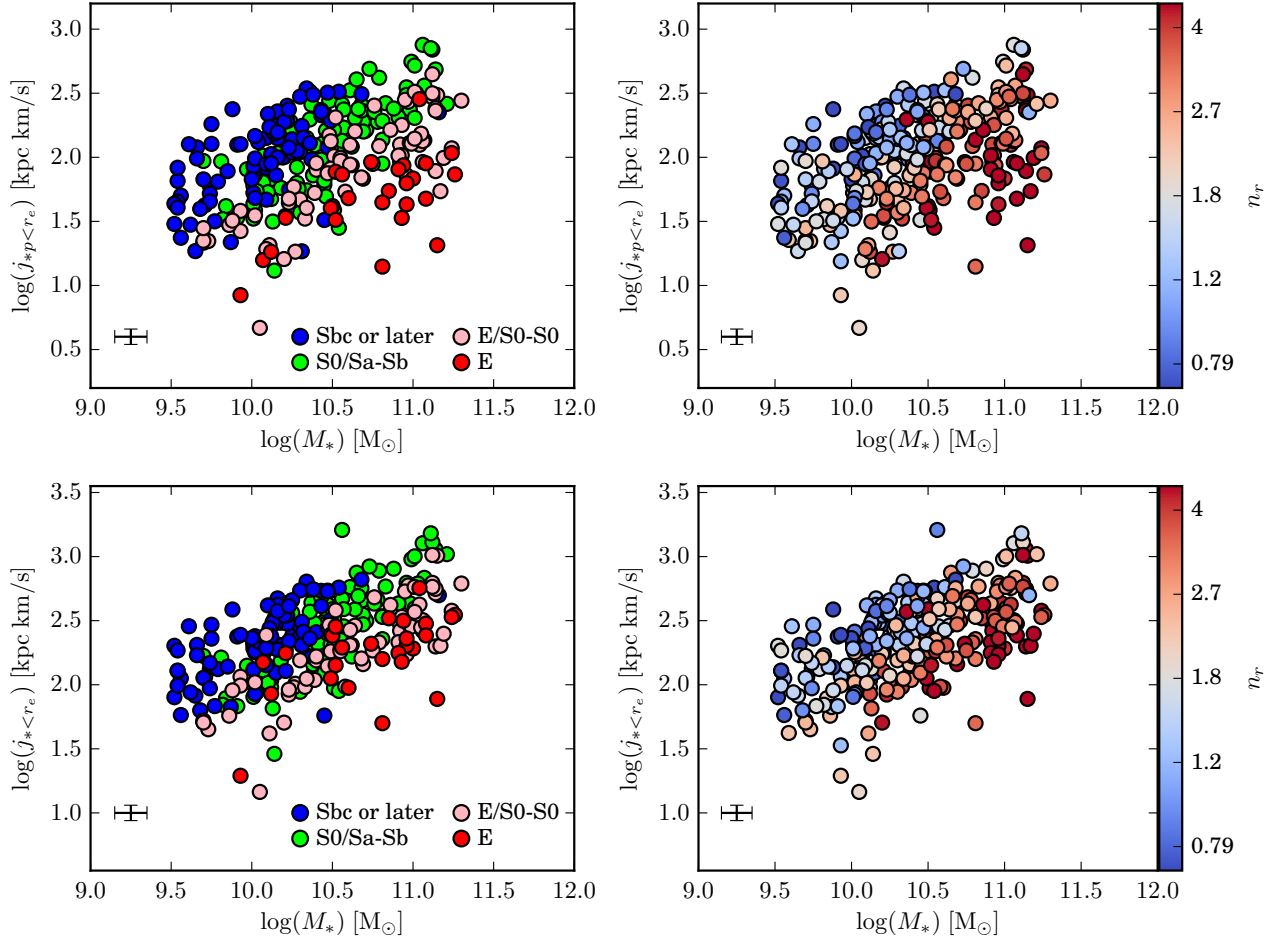


**Figure 2.** The stellar mass versus projected ( $j_{*p}$ , top) and intrinsic ( $j_*$ , bottom) stellar specific angular momentum for SAMI systems. Galaxies are colour-coded by visual morphology and  $r$ -band Sérsic index in the left and right panels, respectively. Errorbars indicate mean statistical errors (i.e., not including uncertainty on inclination correction).

late- and early-type galaxies could simply be a consequence of the fact that  $j_*$  is weighted by luminosity and not stellar mass. Since  $j_*$  is a normalised quantity, it is not the absolute value of the mass-to-light ratio that matters<sup>3</sup>, but its radial gradient. In particular, as massive late-type galaxies have steeper negative gradients (i.e., lower mass-to-light ratios in the outer parts) than early-type systems (Tortora et al. 2011), we could be weighting the outer parts of disks too much, thus significantly overestimating their angular momentum. In order to test this scenario, we estimated  $j_*$  for our galaxies by assuming various mass-to-light ratio gradients. We find that even for an unrealistically large difference of 0.4 dex in the gradients of late- and early-type galaxies (the typical value is not greater than  $\sim 0.2$ - $0.3$  dex for the stellar mass range of our sample; see Tortora et al. 2011), the value of  $j_*$  changes on average by no more than 0.07 dex. This is a factor of four smaller than the typical difference between pure disks and late-types with bulges alone, and seven times smaller than the average difference between late-type

disks and S0 (see also Fall & Romanowsky 2013, hereafter FR13). Thus, we can definitely exclude that our trends are simply a result of an age or metallicity effect which directly impact the estimate of  $j_*$ .

Lastly, as the typical seeing of the SAMI observations used in this work is of the order of  $2.2''$ , beam smearing can have a non-negligible effect on the shapes of the rotation curves (Cecil et al. 2015) and light distributions of our galaxies. While the decrease in velocity could lead to an underestimate of  $j$ , the broadening of the light distribution would (at least partially) balance this effect, reducing the importance of beam smearing. Moreover, at fixed seeing, the effect of beam smearing depends on the light distribution as well as on the gradient of the velocity field within one effective radius. As late-type galaxies have generally larger velocity gradients and shallower light profiles than early-types, beam smearing could mainly artificially reduce (at fixed stellar mass) the difference in  $j$  between disks and bulge dominated systems. Thus, it is unlikely that our main conclusion (i.e., the role of morphology in the scatter of the  $M_*$ - $j_*$  relation) is just a consequence of beam smearing. This is also confirmed in Sec. 5, where we compare our

<sup>3</sup> Assuming that our stellar mass estimates described in Sec. 2.2 properly take into account the variation of mass-to-light ratio with morphology.

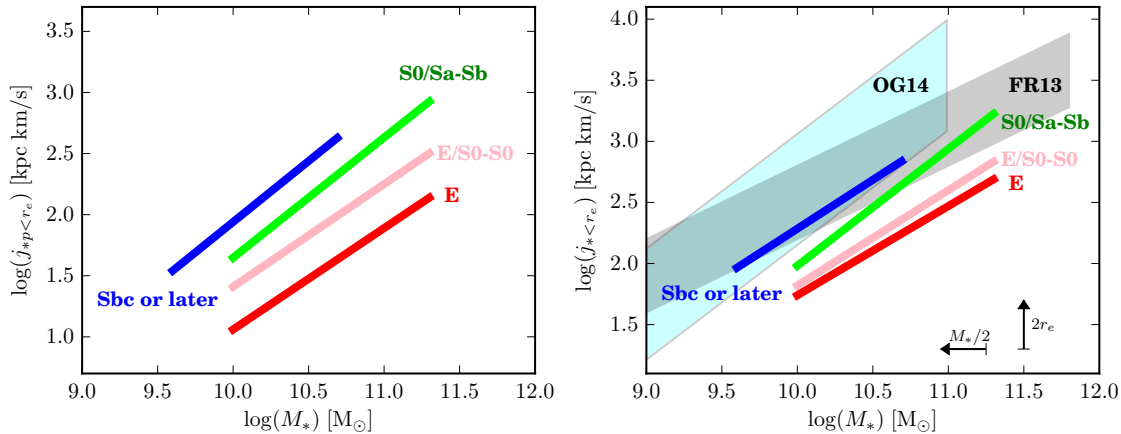


**Figure 3.** The linear fits for the  $M_*$ - $j_{*p}$  (left) and  $M_*$ - $j_*$  (right) relations split by morphological type. The cyan and grey regions show the range covered by the relations obtained by OG14 (including galaxies with bulge-to-total ratio between 0 and 0.3) and Fall & Romanowsky 2013 (FR13, from disks to bulges), respectively. We remind the reader that, for pure ellipticals, the  $M_*$ - $j_*$  relation must be considered as an upper limit, because our inclination correction is likely overestimating the projection effects in these objects. The vertical offset between previous studies and this work is due to the fact that we trace  $j$  only out to one effective radius. Indeed, the black arrows on the bottom-right corner of the right panel indicate how we can expect our relations to shift if we either plot  $j_{* < r_e}$  as a function of half of the stellar mass of our galaxies (i.e., approximately the stellar mass included within one effective radius) or measure  $j_*$  up to  $2 \times r_e$ .

observations with the predictions of (beam smearing-free) simulations.

Using numerical simulations, Wu et al. (2014) found that, when random errors become comparable to the amplitude of the line-of-sight velocity, the derived angular momentum can be artificially boosted. This effect seems to be more prominent in slow rotators. As mentioned in Sec. 2.1, our tests have not shown the presence of any systematic biases in the recovered line-of-sight velocity. However, even if this effect is present in our data, it would preferentially affect slow-rotating systems, artificially reducing the difference between high and low angular momentum galaxies. Thus, the main conclusions of this work would not change.

The importance of morphology (or bulge-to-total ratio) in the scatter of the  $M_*$ - $j_*$  relation has recently been reported by RF12 and OG14. Our work confirms this finding for a larger sample (a factor of  $\sim 3$  more than RF12 and a factor of  $\sim 20$  more than OG14) and, most importantly, focuses on the effect of  $j_*$  within one effective radius, while previous work investigated the total specific angular momentum. Thus, the trends shown here imply that the link between stellar kinematics and morphology is already well established in the inner parts of galaxies.

This is not entirely surprising as the contribution of bulges to both the surface brightness profile and kinematical properties of galaxies is much more dramatic in the inner parts, which are usually well inside one effective radius. In Fig. 3 we compare our  $M_*$ - $j_*$  relations for different morphologies with those found by FR13 (grey area) and OG14 (cyan area). For FR13, the area highlighted is delimited by the  $M_*$ - $j_*$  relations for disks and bulges, while for OG14 we show the range obtained for bulge-to-total ratios varying from 0 to 0.3 (the OG14 sample does not include early type galaxies). The values presented in FR13 are preferred to those in RF12, as stellar mass estimates took into account the variation of mass-to-light ratio with morphological type.

Interestingly, the slope of our  $M_*$ - $j_*$  relation is intermediate between those of FR13 and OG14, although in general closer to the value obtained by FR13 ( $\sim 0.6$ ) than OG14 ( $\sim 1$ ). However, our best-fitting values should be taken with a grain of salt since, as discussed above, our sample is not complete. Thus, we cannot exclude the presence of a selection bias which could affect the slope of our relation. We stress that the most important finding here is not the slope of the relation, but the fact that its scatter is correlated with morphology.

What makes our results significantly different from previous work is the intercept of the relation, which is significantly offset towards lower specific angular momentum. As explained above, this is expected since we are tracing  $j_*$  within one effective radius, thus missing the majority of the total angular momentum in galaxies, which is stored in the outer parts (RF12). We can test this for less than one third of our sample ( $\sim 80$  galaxies), for which we can estimate  $j_*$  at both one and two effective radii. We find that  $j_{* < 2r_e}$  is  $\sim 0.4$  dex higher than  $j_{* < r_e}$ , making our results much more consistent with RF12 and OG14. Similarly, if we plot  $j_*$  as a function of the stellar mass contained in one effective radius, our lines would shift by  $\sim 0.3$  dex (black arrow in the right panel of Fig. 3) making them consistent with previous estimates.

Lastly, it is interesting to note that the slope of our  $M_*$ - $j_*$  relation, as well as the observed spread as a function of morphology, is in line with the recent predictions from cosmological simulations (e.g., Teklu et al. 2015; Genel et al. 2015; Pedrosa & Tissera 2015; Zavala et al. 2015). However, all current theoretical works are focused on the total  $j_*$ , and do not investigate the  $M_*$ - $j_*$  relation within one effective radius.

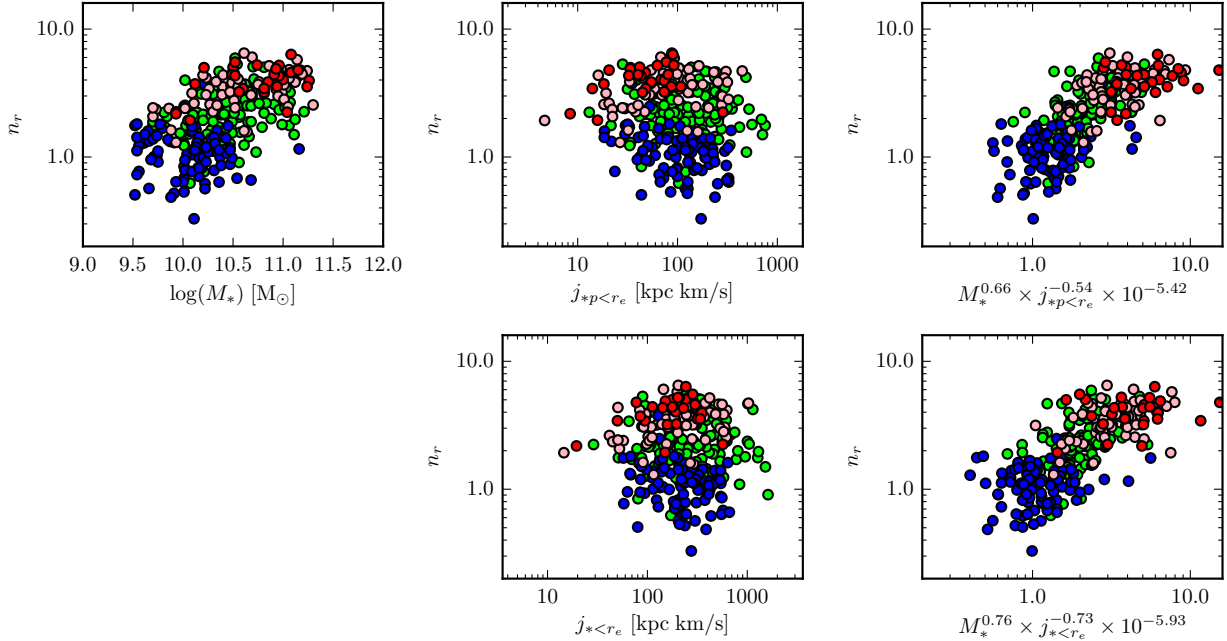


**Figure 4.** Projections of the  $M_*$ - $j_*$ - $n_r$  plane. The top row shows, from left to right, the  $M_*$ - $n_r$ ,  $j_{*p}$ - $n_r$ , and the projection that minimises the scatter in  $n_r$ . The bottom row is the same as the top row, but for the intrinsic  $j_*$ . Symbols are color-coded by morphological type as in Fig. 2.

**Table 1.** Fits to the  $M_*$ - $j$  relations and to the  $M_*$ - $j$ - $n_r$  and  $M_*$ - $j$ - $\lambda_R$  planes. Scatters (rms) are orthogonal to the best fit.

$\log(j/\text{kpc km s}^{-1}) = a \times \log(M_*/M_\odot) + b$					
$j_{*p}$	$a$	$b$	$rms$	$N_{gal}$	
All	$0.72 \pm 0.06$	$-5.49 \pm 0.64$	0.27	297	
E	$0.83 \pm 0.18$	$-7.24 \pm 1.98$	0.21	26	
E/S0 – S0	$0.84 \pm 0.07$	$-6.99 \pm 0.80$	0.17	67	
S0/Sa – Sb	$0.98 \pm 0.08$	$-8.19 \pm 0.81$	0.16	112	
Sbc or later	$1.00 \pm 0.12$	$-8.03 \pm 1.26$	0.18	86	
$j_*$					
All	$0.64 \pm 0.04$	$-4.31 \pm 0.46$	0.22	297	
E	$0.73 \pm 0.18$	$-5.56 \pm 1.88$	0.21	26	
E/S0 – S0	$0.78 \pm 0.06$	$-5.98 \pm 0.68$	0.15	67	
S0/Sa – Sb	$0.96 \pm 0.07$	$-7.58 \pm 0.73$	0.14	112	
Sbc or later	$0.80 \pm 0.09$	$-5.71 \pm 0.89$	0.14	86	
$j_{p\ gas}$					
All	$0.68 \pm 0.03$	$-4.75 \pm 0.27$	0.32	397	
$j_{gas}$					
All	$0.65 \pm 0.02$	$-4.12 \pm 0.23$	0.28	397	
$\log(j/\text{kpc km s}^{-1}) = a \times \log(M_*/M_\odot) + b \times \log(n) + c$					
	$a$	$b$	$c$	$rms$	$N_{gal}$
$j_{*p}$	$1.22 \pm 0.07$	$-1.86 \pm 0.13$	$-10.09 \pm 0.73$	0.13	297
$j_*$	$1.05 \pm 0.06$	$-1.38 \pm 0.10$	$-8.18 \pm 0.56$	0.12	297
$\log(j/\text{kpc km s}^{-1}) = a \times \log(M_*/M_\odot) + b \times \log(\lambda_R) + c$					
	$a$	$b$	$c$	$rms$	$N_{gal}$
$j_{*p}$	$0.70 \pm 0.02$	$1.41 \pm 0.04$	$-4.64 \pm 0.22$	0.05	297
$j_*$	$0.70 \pm 0.03$	$1.13 \pm 0.05$	$-4.47 \pm 0.26$	0.08	297

### 3.1.1 The central stellar specific angular momentum as a driver of morphology

Following RF12 and OG14, the results presented in Fig. 2 and 3 confirm that  $M_*$ ,  $j_*$  and morphology form a plane, and

we can interpret the mix of galaxy morphologies as physically related to the spread in  $j_*$  present in the local galaxy population at fixed stellar mass. The natural consequence of this result is that we can also look into the possibility of expressing morphological parameters such as Sérsic and concentration indices as a function of stellar mass and specific angular momentum.

To do so, we fit a plane to  $M_*$ ,  $j_*$  and  $n_r$ . We performed this exercise on both the projected and intrinsic relations. The results are presented in Fig. 4 and compared to the  $M_*$ - $n_r$ , and  $j_*$ - $n_r$  relations. The parameters for the best-fitting plane are presented in Table 1. It is clear that not only we recover the Sérsic index with  $\sim 0.20$  dex scatter (orthogonal scatter of  $\sim 0.13$  dex), but also that the combination of  $M_*$  and  $j_*$  performs significantly better than  $M_*$  alone. This confirms that both the mass and the kinematic properties of galaxies play an important role in setting their stellar density distributions. Similar results are obtained if, instead of the Sérsic index, we use the SDSS-based concentration index. The fact that the scatter of the projected and intrinsic version of the plane are nearly the same confirms that our main conclusions are not an effect of inclination. Ideally, this exercise should be performed using the bulge-to-total mass ratio because this is the best (i.e., more physically motivated) photometric-based morphological indicator. Unfortunately, reliable bulge-to-disk decompositions are not yet available for our entire sample, so we have to postpone this analysis to future work.

Admittedly, the scatter in the  $M_*$ - $j_*$ - $n_r$  plane is significantly larger than the scatter observed in the fundamental plane ( $\sim 0.06$ - $0.08$  dex e.g., Jorgensen et al. 1996; Bernardi et al. 2003; Hyde & Bernardi 2009; Cappellari et al. 2013) and other structural and dynamical scaling relations

(e.g., Faber & Jackson 1976; Tully & Fisher 1977; Catinella et al. 2012; Cortese et al. 2014). However, these relations are usually calibrated on pruned samples including only pre-selected morphological types (but see Cortese et al. 2014), whereas the  $M_*-j_*-n_r$  plane applies to all galaxies. Moreover, the scatter along the direction of  $n$  is similar to the typical scatter of the main sequence of star-forming galaxies (Dutton et al. 2010) and of the empirical relations used to predict the gas content of galaxies (Cortese et al. 2011; Catinella et al. 2013). Lastly, the orthogonal scatter of the plane is significantly smaller than that of the  $M_*-j_*$  relation, confirming quantitatively the link between stellar mass, angular momentum and morphology.

### 3.2 The gas specific angular momentum within one effective radius

One limitation of the analysis presented above is that SAMI data allow us to trace  $j_*$  only in galaxies with  $M_* \gtrsim 10^{9.5} M_\odot$ . Despite this, we can extend this study to lower stellar masses by measuring the kinematics of the ionized gas instead of the stellar component. Indeed, H $\alpha$  emission is detected in a significant fraction of galaxies below  $M_* \sim 10^{9.5} M_\odot$  (see Fig. 1), allowing us to look at the relation between stellar mass, specific angular momentum and morphology across almost three orders of magnitude in stellar mass. The ionised gas specific angular momentum ( $j_{gas}$ ) has been estimated from H $\alpha$  velocity maps following Eq. 6 and 7. We use the H $\alpha$  intensity map to determine  $F_k$  in each spaxel, as we consider this a better proxy for the gas mass distribution in our galaxies than the optical continuum emission. However, similar results are obtained if the stellar emission is used instead.

In Fig. 5, we show the  $j_{p\ gas}$  (top) and  $j_{gas}$  (bottom) as a function of  $M_*$ . As in Fig. 2, galaxies are colour-coded according to their  $r$ -band Sérsic index. We do not colour-code galaxies for visual morphology since, in our sample, nearly all galaxies below  $M_* \sim 10^{10} M_\odot$  are classified as pure disks (see also Fig. 2 in Cortese et al. 2014).

The strong correlation between  $M_*$  and  $j_{gas}$  extends across the entire range of stellar masses covered by this work, with a scatter slightly larger than that observed for the stellar component (see Table 1). This is likely due to the use of the H $\alpha$  line emission, as its distribution is much more irregular than the stellar continuum. The slope of the  $M_*-j_{gas}$  relation ( $\sim 0.65$ ) is consistent with the one obtained for  $j_*$  ( $\sim 0.64$ ).

Interestingly, the values of stellar and gas specific angular momentum (and hence the intercept of the  $M_*-j_*$  relation) are significantly different, with  $j_{gas}$  being systematically larger than  $j_*$  (average  $j_{gas}/j_*$  ratio  $\sim 0.10$  dex, obtained using those galaxies for which we can estimate both  $j_{gas}$  and  $j_*$ ). This discrepancy is consistent with (and a direct consequence of) the difference in gas and stellar rotational velocities already noticed by Cortese et al. (2014) in SAMI data, and it is likely the effect of asymmetric drift. Thus, it is clear that, in order to properly compare galaxies of different types, we must compare  $j$  for the same baryonic component.

Contrary to what is observed for the case of  $j_*$ , Sérsic index (or any other indicator of galaxy morphology) is not playing a critical role in driving the scatter of the  $M_*-j_{gas}$

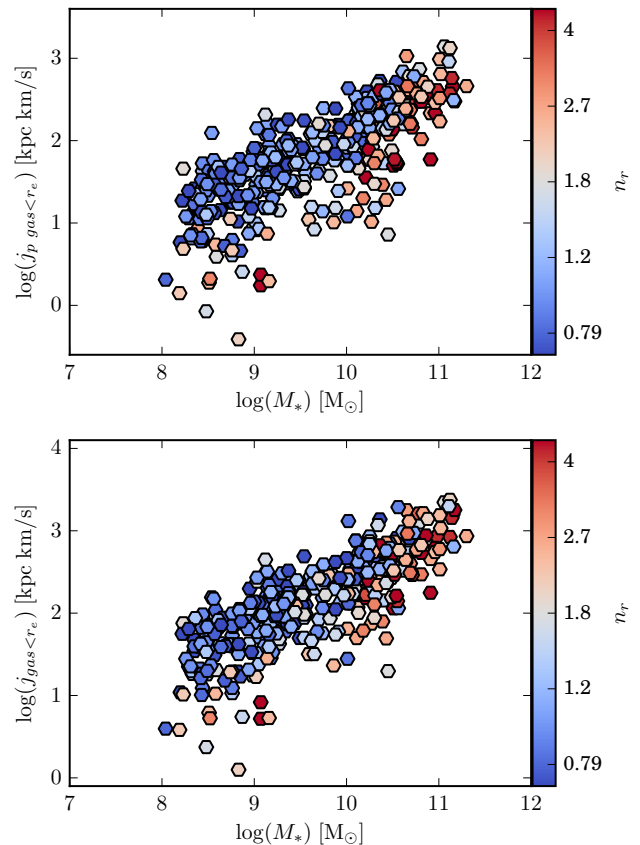


**Figure 5.** The  $M_*-j_{p\ gas}$  (top) and  $M_*-j_{gas}$  (bottom) relations for SAMI galaxies. Galaxies are colour-coded by  $r$ -band Sérsic index.

relation. Only if we focus on massive galaxies, do we recover similar trends as those shown in Figs. 2 and 4 for the stellar component. Unfortunately, because we do not detect H $\alpha$  emission in many massive early-type, bulge-dominated galaxies (see Fig. 1), we are missing a crucial part of the parameter space. Moreover, while both disk and bulge contribute to  $j_*$ , it is likely that  $j_{gas}$  mainly traces the dynamics of the disk. Consequently, the gas angular momentum is not an ideal quantity to investigate the relation between kinematics and morphology in the high stellar mass regime.

Intriguingly, there is marginal evidence for an increase in the scatter in the  $M_*-j_*$  relation with decreasing stellar mass. If confirmed, this may support the findings of high turbulence (sometimes comparable to the rotation velocities) in the ISM of dwarf galaxies (Cortese et al. 2014; Simons et al. 2015; Wheeler et al. 2015). Moreover, the fact that the scatter in the  $M_*-j_{gas}$  relation is similar to that of the  $M_*-j_*$  relation (and significantly larger than the observational uncertainty) suggests that the dynamical state of the gas is not strongly correlated with the stellar light distribution in a galaxy, and that there exist other physical properties of galaxies responsible for the scatter of the  $M_*-j_{gas}$  relation. We will investigate this issue in a future work.

#### 4 THE SPIN PARAMETER

In a theoretical framework, the scatter of the  $M_*$ - $j_*$  relation should, at least partially, reflect the wide range of kinematic properties of dark matter halos of similar mass. Given that during the growth of structures, halos exert tidal torques onto each other, it is natural to expect that the degree of rotational support can vary across a large dynamical range. However, the exact connection between the angular momentum of the halo and that of the stars remains an outstanding question.

The importance of ordered motions is usually quantified via the spin parameter  $\lambda$ , which is defined as:

$$\lambda = \frac{J|E|^{1/2}}{GM^{5/2}} \quad (8)$$

where  $J$  is the angular momentum,  $E$  is the total mechanical (potential plus kinetic) energy of the system,  $G$  is the gravitational constant and  $M$  is the total mass. Thus, the scatter of the  $M_*$ - $j_*$  relation may correlate with  $\lambda$ , and  $\lambda$  may somehow regulate galaxy morphology (e.g., Fall & Efstathiou 1980; Dalcanton et al. 1997; Mo et al. 1998; Boissier & Prantzos 2000; Zavala et al. 2008, but see also Scannapieco et al. 2009; Romanowsky & Fall 2012; Sales et al. 2012). Intriguingly, the width of the spin parameter distribution predicted by simulations is  $\sim 0.22$  dex (e.g., Bullock et al. 2001), very close to the scatter of our  $M_*$ - $j_*$  relation.

Unfortunately, estimating  $\lambda$  from observations is extremely challenging. Not only physical quantities such as total energy and total mass are not easily derived from observations, but also Eq. 8 strictly applies to the dark matter halo, and the ratio between the spin of the halo and that of the baryons can easily vary during the evolutionary history of galaxies (Scannapieco et al. 2009; Sharma et al. 2012; Teklu et al. 2015).

In the last few years, the advent of integral field spectroscopy has made the  $\lambda_R$  parameter (Emsellem et al. 2007, 2011) the most commonly-used proxy for stellar spin parameter (see Appendix A in Emsellem et al. 2007):

$$\lambda_R = \frac{\sum_{k=1}^n F_k R_k |V_{k \text{ los}}|}{\sum_{k=1}^n F_k R_k \sqrt{V_{k \text{ los}}^2 + \sigma_k^2}} \quad (9)$$

where  $V_{k \text{ los}}$  and  $\sigma_k$  are the line-of-sight and dispersion velocities in each spaxel, respectively, and  $F_k$  and  $R_k$ <sup>4</sup> are as in Eq. 6. It is important to note that  $\lambda_R$  is a projected quantity and, at face value, does not take into account the effect of inclination. This parameter was originally defined for early-type galaxies, for which inclinations are notoriously uncertain, and it has to be combined with the observed galaxy ellipticity to allow a proper separation between fast and slow rotators. Despite this possible bias,  $\lambda_R$  is becoming commonly used for galaxies of all morphologies (Jimmy et al. 2013; Pracy et al. 2013; Tapia et al. 2014; Falc3n-Barroso et al. 2015; Fogarty et al. 2015), thus it is interesting to see

<sup>4</sup> We note that, although consistent with Fogarty et al. (2014, 2015), our definition of  $\lambda_R$  is different from the original definition by Emsellem et al. (2007). Namely, it uses de-projected instead of projected radii. However, this difference does not significantly affect our findings.

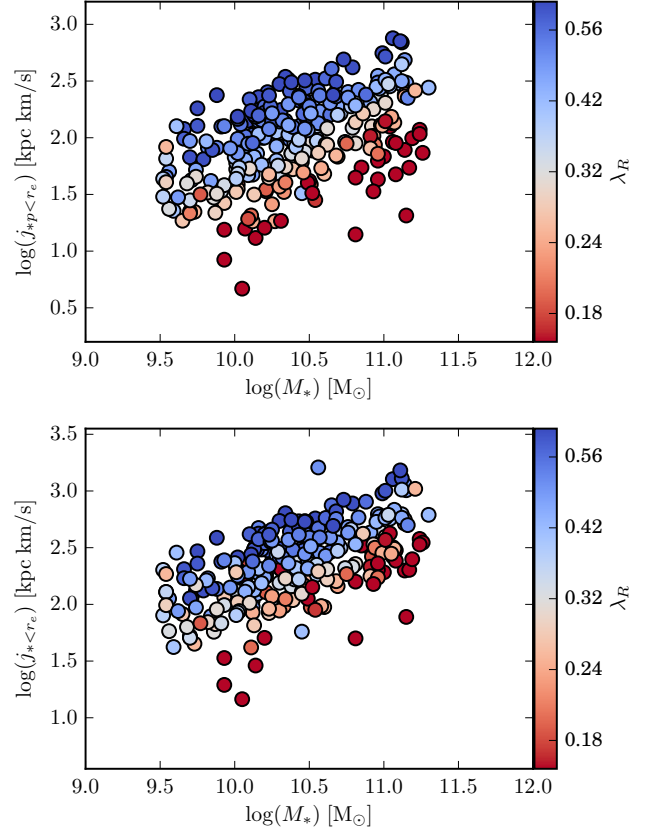


**Figure 6.** The  $M_*$ - $j_{*p}$  (top) and  $M_*$ - $j_*$  (bottom) relations with galaxies colour-coded by stellar spin parameter  $\lambda_R$ .

how the results presented above can be interpreted in the context of this parameter.

Fig. 6 shows the  $M_*$ - $j_*$  relation, this time colour-coded by values of  $\lambda_R$ . As expected, since  $j_*$  and  $\lambda_R$  are not independent quantities, we find that the scatter in the relation correlates strongly with  $\lambda_R$ . Indeed, the scatter in the best-fitting  $M_*$ - $j_*$ - $\lambda_R$  plane is  $\sim 0.08$  dex, significantly smaller than in the case of the Sérsic index (see Table 1). Remarkably, the best-fitting coefficients are very close to  $j_* \sim M_*^{2/3} \times \lambda_R$ , which can be recovered analytically (see e.g., RF12 and OG14) within the general theoretical framework of Mo et al. (1998), assuming that  $\lambda_R$  is proportional to halo spin parameter, and a constant halo-to-stellar mass ratio. The projected version of the plane has a scatter significantly smaller than the intrinsic one. This is simply because  $\lambda_R$  is a projected quantity and thus it correlates more tightly with the scatter of the  $M_*$ - $j_{*p}$  relation.

From an observational point of view, since the slope of the  $M_*$ - $j_*$ - $\lambda_R$  plane in the  $\lambda_R$  projection is very close to 1, the tight  $M_*$ - $j_*$ - $\lambda_R$  plane becomes akin<sup>5</sup> to the known relation between  $M_*$  and  $\sqrt{V^2 + \sigma^2}$ , (Cortese et al. 2014), which shows similar scatter ( $\sim 0.1$  dex) and represents a promising

<sup>5</sup> Indeed, if  $j_* \propto \lambda_R M_*^a$  by simply dividing  $j_*$  and  $\lambda_R$ , the equation for the plane can be re-expressed as  $M_* \propto \left( \frac{\sum_{k=1}^n F_k R_k |V_{k \text{ los}}|}{\sum_{k=1}^n F_k} \right)^{1/a}$ .

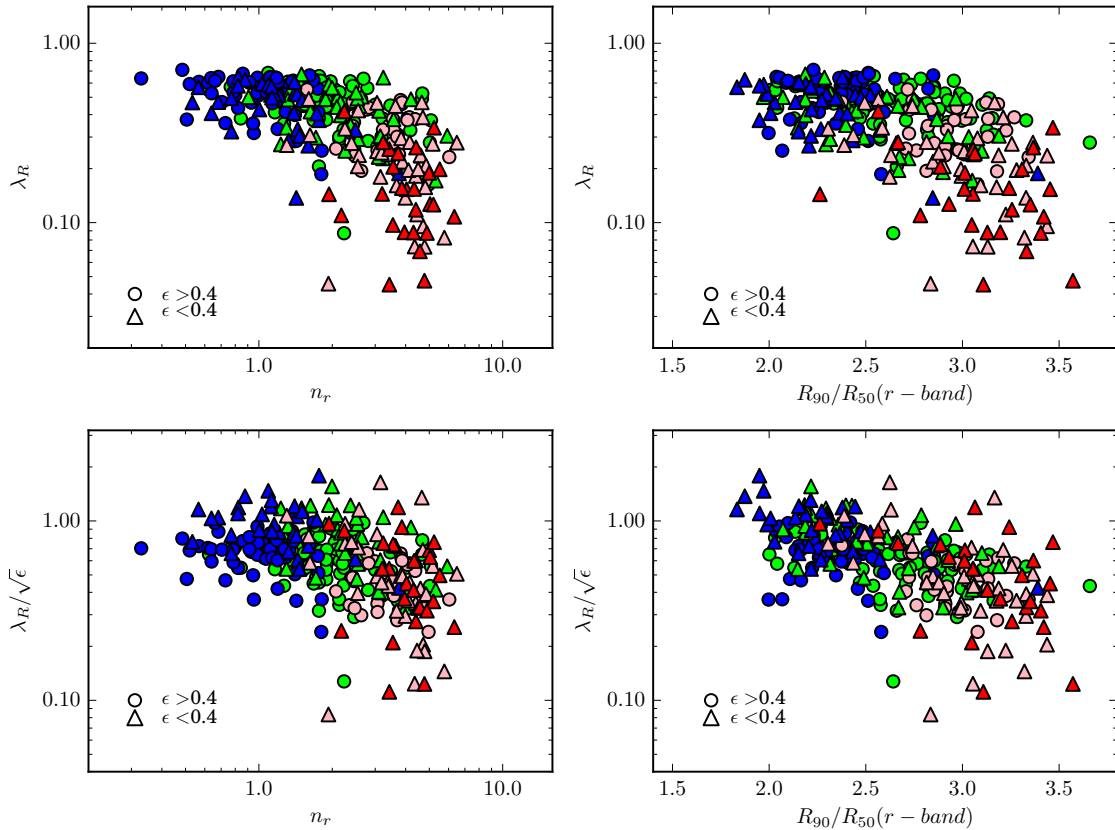


**Figure 7.** The stellar  $\lambda_R$ - $n_r$  (top-left),  $\lambda_R$ - $R_{90}/R_{50}$  (top-right),  $\lambda_R/\sqrt{\epsilon}$ - $n_r$  (bottom-left),  $\lambda_R/\sqrt{\epsilon}$ - $R_{90}/R_{50}$  (bottom-right) relations for our sample. Points are colour-coded by visual morphology as in Fig. 2. Circles and triangles indicate galaxies with ellipticities larger and smaller than 0.4, respectively.

unified dynamical scaling relation valid for galaxies of all regular morphological types.

The role played by  $\lambda_R$  in the scatter of the  $M_*$ - $j_*$  relation, combined with the results of Sec. 3, implies that  $\lambda_R$  should correlate with indicators of optical morphology such as  $n_r$  and concentration index. This correlation is investigated in the top panel of Fig. 7. Although  $\lambda_R$  clearly correlates with both quantities (Spearman correlation coefficient  $\sim -0.6$ ), the relations show quite a large amount of scatter, as recently highlighted by Fogarty et al. (2015) using a smaller sample of cluster galaxies from the SAMI pilot survey (see also Falc3n-Barroso et al. 2015). This is particularly true for high S3ersic and concentration indices, where there is almost no correlation between  $\lambda_R$  and optical morphology. Interestingly, this is the typical parameter space occupied by the population of ‘slow-rotators’ investigated by the ATLAS<sup>3D</sup> survey (Cappellari et al. 2011a; Emsellem et al. 2011), for which it has been claimed that optical morphology does not represent a good proxy for their kinematic properties (Krajinovi3c et al. 2013).

However, part of the scatter and non linearity in the  $\lambda_R$ - $n_r$  (left) and  $\lambda_R$ - $R_{90}/R_{50}$  relations is likely just a consequence of the fact that  $\lambda_R$  is a projected quantity. As shown in Fig. 7, the vast majority of the outliers from the main relation are galaxies with ellipticities smaller than 0.4 (triangles in Fig. 7). Moreover, if we try to account for the effect of inclination by simply plotting  $\lambda_R/\sqrt{\epsilon}$  instead of  $\lambda_R$ , the

correlation becomes more linear, in particular for the concentration index. Of course, this is a crude way to correct for inclination and to properly quantify projection effects, something outside the scope of this paper, we do require detailed dynamical modeling. Indeed, not only the inclination but also the anisotropy of the velocity field are needed to correct both line-of-sight and dispersion velocities.

Thus, at this stage, we can at least safely conclude that, excluding slow-rotators, there is a good correlation between optical morphology and  $\lambda_R$ , with the value of the spin parameter decreasing with the increase of stellar concentration.

## 5 COMPARISON WITH MODELS

The most natural interpretation of our results is that the stellar density distribution in galaxies, and thus their morphology, is a direct manifestation of the contribution of ordered motions to the dynamical support of the system. The larger the contribution of dispersion, the more centrally concentrated the stars are and the more closely the galaxy resembles to a bulge-dominated system. This is consistent with previous works that found a correlation between the  $V/\sigma$  ratio and galaxy morphology (Courteau et al. 2007; Catinella et al. 2012).

However, it is important to make sure that such a scenario is not only qualitatively, but also quantitatively consistent with our findings. Thus, in this section we compare our

results with the predictions of the theoretical model developed by Bekki (2013) for isolated galaxies. A detailed comparison with numerical simulations in a cosmological context will be the focus of a future paper. The immediate advantage of using the Bekki (2013) code is that, thanks to its high resolution ( $3 \times 10^5 M_\odot$  in mass and 193 pc in size), we can analyse the output of the simulation using the same tools used for the SAMI data, and extract physical quantities in a consistent way. The main goal of this exercise is simply to test if the scatter in the  $M_*$ - $j_*$  relation and the relation between stellar concentration and  $\lambda_R$  can be reproduced by increasing the mass of a fully dispersion supported bulge component.

We use the realisations of disk galaxies presented in Bekki (2014). Briefly, a disk galaxy is assumed to consist of a dark matter halo, a stellar and gas disk, and a stellar bulge. The gas-to-stellar mass ratio and the total stellar-to-dark matter disk mass ratio are set to be 0.1 and 0.06, respectively.

The initial density profile of the dark matter halo is assumed to be a Navarro-Frenk-White (NFW; Navarro et al. 1997) profile with concentration set to 10. The bulge component has a Hernquist (1990) density profile evaluated up to five scale lengths, with the bulge scale length set to 0.35 times that of the disk. The bulge is assumed to be non rotating and to have an isotropic velocity dispersion. The radial velocity dispersion is given according to the Jeans equation for a spherical system, including also the mass contribution from the halo.

The radial ( $R$ ) and vertical ( $Z$ ) density profiles of the stellar disk are assumed to be proportional to  $\exp(-R/R_0)$  extending up to 5 scale lengths, and to  $\text{sech}^2(Z/Z_0)$  with scale length  $Z_0 = 0.2R_0$ , respectively. The size of the gas disk is twice that of the stellar one.

In addition to the rotational velocity caused by the gravitational field of the disk, bulge, and dark halo components, the initial radial and azimuthal velocity dispersions are assigned to the disk component according to the epicyclic theory with Toomre's parameter  $Q$  (Toomre 1964). Here we choose  $Q=3.0$ , which appears to best match the observed stellar velocity dispersion of SAMI galaxies.

We consider models for two values of bulge-to-disk stellar mass ratio ( $B/D=0$  and 1) and three total dark matter masses (1, 0.3 and  $0.1 \times 10^{12} M_\odot$ , corresponding to disk scale lengths of 3.5, 1.9 and 1.1 kpc). For each model we extract line-of-sight velocity, velocity dispersion and stellar density maps using a mesh size of 0.5 kpc, roughly consistent with the typical size of SAMI spaxels, and assuming three inclinations: 10, 50 and 80 degrees. 'Observed' total stellar masses, effective radii, ellipticities and concentration indices<sup>6</sup> are estimated directly from the stellar mass distribution maps by fitting isophotal ellipses, following the technique described in Cortese et al. (2012). Specific angular momentum and  $\lambda_R$  are then extracted within one effective radius following Eq. 7 and 9, and using exactly the same software adopted for the SAMI data. The only difference be-

tween simulated and observed parameters is that simulated  $j_*$  and  $\lambda_R$  are weighted by stellar mass instead of luminosity.

In Fig. 8, we compare the model predictions with the SAMI data on the  $M_*$ - $j_*$  (left) and the  $\lambda_R$ - $R_{90}/R_{50}$  (right) relations. The beige and orange points show the  $B/D=0$  and  $B/D=1$  cases, respectively. The agreement between simulated and real data is encouraging. Although the slope of the  $M_*$ - $j_*$  relation is a direct consequence of the modeling (i.e., of the assumptions made on the mass and velocity profiles), it is interesting to see that we are able to quantitatively reproduce the difference between the pure-disk and bulge plus disk models not only in the  $M_*$ - $j_*$  relation, but also in the  $\lambda_R$ - $R_{90}/R_{50}$  plot. The difference between models with different inclinations (circles, diamonds and triangles in Fig. 8) also gives an idea of the systematic uncertainty in our inclination correction. In particular, it is not surprising that the inclination correction is much more erroneous for bulge dominated spirals than for pure disks. For inclined early-type disks, the best-fitting ellipses to the entire galaxy have generally a smaller ellipticity than the disk alone, significantly affecting the accuracy of our inclination correction. Although Fig. 8 indicates that our inclination correction might underestimate  $j_*$  for face-on bulge-dominated galaxies, we note that just a couple of galaxies in our S0 sample are face-on, whereas the vast majority of our targets have inclinations greater than 40 degrees where our correction appears to work properly.

In summary, it is clear that the presence of prominent, fully dispersion supported bulges can quantitatively reproduce the offset between late- and early-type galaxies in the  $M_*$ - $j_*$  relation and the trend seen between spin and concentration (see also RF12). Thus, this comparison confirms that the results presented in this paper can be interpreted as a simple manifestation of the physical link between the stellar density distribution and kinematics in galaxies across the Hubble sequence. The next step is therefore to compare our findings to the predictions of cosmological simulations to follow the growth of mass and angular momentum in galaxies in a self-consistent fashion (e.g., Snyder et al. 2015; Genel et al. 2015; Teklu et al. 2015).

## 6 DISCUSSION & CONCLUSIONS

The analysis presented in this paper provides quantitative evidence that both the stellar and gas specific angular momentum of galaxies measured within one effective radius strongly correlate with stellar mass. The slope of the relation across the whole sample ( $\sim 0.64$ ) is remarkably close to the value expected from analytical models (2/3). However, given that our sample is not complete, future confirmation for the exact slope of the  $M_*$ - $j_*$  relation is needed.

We show that for stellar masses  $\gtrsim 10^{9.5} M_\odot$ , the scatter in the  $M_*$ - $j_*$  relation is related to the stellar light distribution, hence morphology, of galaxies. Compared to previous works, not only do we take advantage of significantly larger number statistics, but also, thanks to SAMI integral field spectroscopy, we are able to quantify the specific angular momentum using exactly the same technique for all galaxies in our sample.

One of the most important implications of our findings is that, from a statistical point of view, we can quantify

<sup>6</sup> In order to be consistent with observations, effective radii are obtained by fitting isophotal ellipses, while the concentration index comes from the radii obtained from fitting circular apertures to the simulated data.

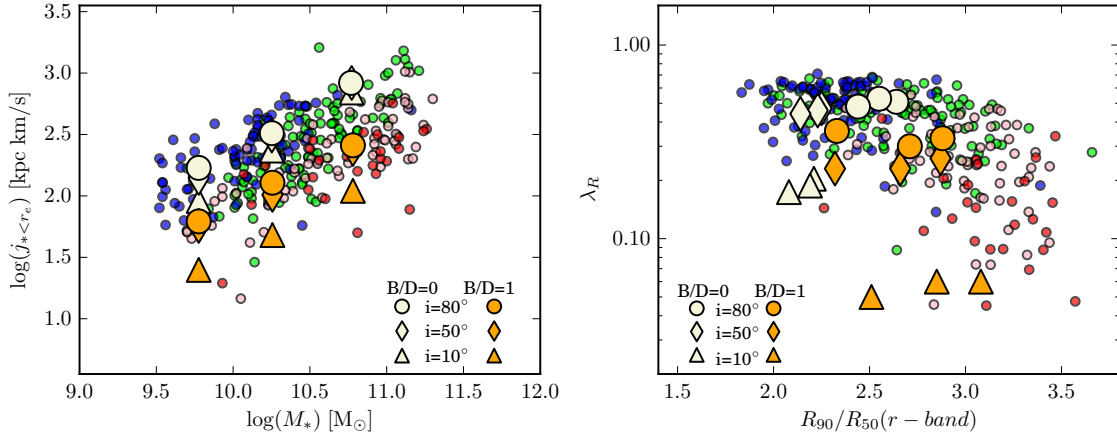


**Figure 8.** Comparison between the observed  $M_*$ - $j_*$  (left) and  $\lambda_R$ - $R_{90}/R_{50}$  (right) relations (small circles) and the predictions of the model by Bekki (2013, 2014; large symbols). Beige and orange symbols indicate models for pure disks and disk galaxies with B/D ratio of 1, respectively. For each model, large circles, diamonds and triangles show inclinations of 80, 50 and 10 degrees, respectively. SAMI galaxies are colour-coded by their visual morphology as in Fig. 2.

galaxy morphology via the kinematic properties of galaxies: once we know the stellar mass and specific angular momentum of an object, we can predict what its stellar light profile will be. In other words, galaxies lie on a tight plane defined by their Sérsic index, stellar mass, and specific angular momentum (see also OG14). A similar conclusion is reached if  $j_{gas}$  is used instead of  $j_*$ . However, as the presence of H $\alpha$  emitting gas up to one effective radius is not widespread in early-type systems, it is much more challenging to use  $j_{gas}$  to calibrate the  $M_*$ - $j$ - $n_r$  plane.

We show that, from a physical point of view, the scatter in the  $M_*$ - $j_*$  relation is simply a consequence of the fact that, at fixed stellar mass, the contribution of ordered motions to the dynamical support of galaxies varies by at least a factor of three. Indeed, the stellar spin parameter  $\lambda_R$  is even more correlated with the scatter in the  $M_*$ - $j_*$  relation. This is quite remarkable considering that  $\lambda_R$  is a projected quantity, not corrected for the effect of inclination. Intriguingly, we find that the correlation between  $\lambda_R$  and morphology seems to break down for bulge-dominated, slow-rotator galaxies, suggesting that at fixed stellar concentration we can have a wide range of spin parameters. However, this could simply be an inclination effect, and further analysis (including accurate inclination corrections) are needed to determine whether or not the stellar density distribution alone is sufficient to isolate slow rotators (Emsellem et al. 2011; Krajnović et al. 2013).

Conversely, the tight relation between spin and Sérsic index observed for the rest of our sample shows that, when we look at their stellar distribution and kinematics, early-type fast rotators and late-type galaxies are not two separate classes of objects, but represent a ‘continuum’ connecting pure-disks to bulge-dominated systems. Given that galaxies with a disk/rotationally-supported component are by far the most common in the local Universe (Emsellem et al. 2011; Kelvin et al. 2014), the ability to link their morphological properties to their kinematics is of critical importance for understanding the origin of the Hubble sequence. For example, as also illustrated by Fogarty et al. (2015), our results imply that, if galaxies are really morphologically trans-

formed, their stellar kinematics should be affected as well. Similarly, if galaxy transformation is simply a result of the quenching of the star formation (and of the consequent fading of the spiral arms), at fixed stellar mass passive galaxies should show the same kinematical properties as star-forming disks. Thus, information on the stellar kinematics of galaxies can allow us to investigate these scenarios, moving beyond relations such as the morphology-density relation. Particularly promising is the ability to investigate the effect of the environment in terms of mass, star formation and angular momentum without the need to split galaxies by morphology, as is currently done even for the so-called kinematic morphology-density relation (Cappellari et al. 2011b).

Although our findings are consistent with theoretical expectations, and with previous observations by RF12 and OG14, they may appear in contradiction with Krajnović et al. (2013), who did not find a correlation between Sérsic index and  $\lambda_R$  for early-type galaxies in ATLAS<sup>3D</sup>. However, it is easy to show that this is simply due to the fact that the ATLAS<sup>3D</sup> sample included only early-type galaxies, thus missing the large family of rotationally supported systems with little or no bulge component. Indeed, if we focus on early-type galaxies only, it is clear from the top row of Fig. 7 that the trend disappears also in our sample, consistently with Fig. 4 in Krajnović et al. (2013). This simply supports the argument that early-type fast rotators and late-type galaxies should be treated as a single population, and it is fully consistent with the proposed revision of the Hubble tuning-fork, where S0s are directly linked to late-type disk galaxies and they are no longer a transition class between spirals and ellipticals (Spitzer & Baade 1951; van den Bergh 1976; Cappellari et al. 2011b; Kormendy & Bender 2012).

In the future, it will be important to extend our results by replacing Sérsic and concentration indices with accurate estimates of bulge-to-disk ratios. As bulge-to-disk decomposition is arguably the most physically motivated imaging-based morphological classification, we should find that the increase in the importance of random motions across the

Hubble sequence is directly related to the increase of the mass in the ‘photometric’ bulge.

Finally, it is important to highlight the limitations of our current analysis in order to avoid dangerous extrapolation of our findings. Firstly, as SAMI data allow us mainly to investigate the inner parts of galaxies, it is possible (and perhaps even expected) that some of our conclusions change once the total (i.e., integrated up to several effective radii) angular momentum is taken into account (Arnold et al. 2014). However, the fact that RF12 reaches similar conclusions by investigating the total specific angular momentum is encouraging. Secondly, due to our limited spatial resolution, we struggle to trace with extreme detail gas and stellar kinematics in the inner 1-2 kpc of our targets. Thus, at this stage, our velocity maps do not allow us to discriminate between the presence of a classical or a pseudo-bulge (Kormendy & Kennicutt 2004) and determine their role in the scatter of the  $M_* - j_*$  relation. This means that velocity maps with kiloparsec or sub-kiloparsec resolution, extending up to the outer edges of galaxies, will be critical for further unveiling the complex connection between galaxy structure and kinematics.

Nevertheless, our work already demonstrates how homogeneous estimates of the stellar and gas angular momentum across all galaxy types allow us to move beyond visual morphology and shed light on the physical origin of the Hubble sequence.

## ACKNOWLEDGMENTS

We thank the referee for a very detailed and constructive report which significantly improved the quality of this manuscript.

LC acknowledges financial support from the Australian Research Council (DP130100664, DP150101734). BC is the recipient of an Australian Research Council Future Fellowship (FT120100660). JTA acknowledges the award of a John Stocker Postdoctoral Fellowship from the Science and Industry Endowment Fund (Australia). MSO acknowledges the funding support from the Australian Research Council through a Future Fellowship Fellowship (FT140100255). SB acknowledges the funding support from the Australian Research Council through a Future Fellowship (FT140101166). AMM acknowledges the support of the Australian Research Council through Discovery project DP130103925.

Part of this work was performed on the gSTAR national facility at Swinburne University of Technology. gSTAR is funded by Swinburne and the Australian Governments Education Investment Fund.

The SAMI Galaxy Survey is based on observations made at the Anglo-Australian Telescope. The Sydney-AAO Multi-object Integral field spectrograph (SAMI) was developed jointly by the University of Sydney and the Australian Astronomical Observatory. The SAMI input catalogue is based on data taken from the Sloan Digital Sky Survey, the GAMA Survey and the VST ATLAS Survey. The SAMI Galaxy Survey is funded by the Australian Research Council Centre of Excellence for All-sky Astrophysics (CAASTRO), through project number CE110001020, and other participating institutions. The SAMI Galaxy Survey website is <http://sami-survey.org/>.

GAMA is a joint European-Australasian project based around a spectroscopic campaign using the Anglo-Australian Telescope. The GAMA input catalogue is based on data taken from the Sloan Digital Sky Survey and the UKIRT Infrared Deep Sky Survey. Complementary imaging of the GAMA regions is being obtained by a number of independent survey programs including GALEX MIS, VST KiDS, VISTA VIKING, WISE, Herschel-ATLAS, GMRT and ASKAP providing UV to radio coverage. GAMA is funded by the STFC (UK), the ARC (Australia), the AAO, and the participating institutions. The GAMA website is <http://www.gama-survey.org/>.

## REFERENCES

- Abraham R. G., Valdes F., Yee H. K. C., van den Bergh S., 1994, *ApJ*, **432**, 75
- Ahn C. P., et al., 2012, *ApJS*, **203**, 21
- Allen J. T., et al., 2015a, *MNRAS*, **446**, 1567
- Allen J. T., et al., 2015b, *MNRAS*, **451**, 2780
- Arnold J. A., et al., 2014, *ApJ*, **791**, 80
- Bacon R., et al., 2001, *MNRAS*, **326**, 23
- Banerji M., et al., 2010, *MNRAS*, **406**, 342
- Bekki K., 2013, *MNRAS*, **432**, 2298
- Bekki K., 2014, *MNRAS*, **438**, 444
- Bell E. F., McIntosh D. H., Katz N., Weinberg M. D., 2003, *ApJS*, **149**, 289
- Bernardi M., et al., 2003, *AJ*, **125**, 1866
- Bershady M. A., Jangren A., Conselice C. J., 2000, *AJ*, **119**, 2645
- Binggeli B., Sandage A., Tammann G. A., 1985, *AJ*, **90**, 1681
- Bland-Hawthorn J., et al., 2011, *Optics Express*, **19**, 2649
- Boissier S., Prantzos N., 2000, *MNRAS*, **312**, 398
- Bryant J. J., Bland-Hawthorn J., Fogarty L. M. R., Lawrence J. S., Croom S. M., 2014, *MNRAS*, **438**, 869
- Bryant J. J., et al., 2015, *MNRAS*, **447**, 2857
- Bullock J. S., Dekel A., Kolatt T. S., Kravtsov A. V., Klypin A. A., Porciani C., Primack J. R., 2001, *ApJ*, **555**, 240
- Cappellari M., Emsellem E., 2004, *PASP*, **116**, 138
- Cappellari M., et al., 2011a, *MNRAS*, **413**, 813
- Cappellari M., et al., 2011b, *MNRAS*, **416**, 1680
- Cappellari M., et al., 2013, *MNRAS*, **432**, 1709
- Catinella B., et al., 2012, *MNRAS*, **420**, 1959
- Catinella B., et al., 2013, *MNRAS*, **436**, 34
- Cecil G., et al., 2015, preprint, ([arXiv:1511.05445](https://arxiv.org/abs/1511.05445))
- Chabrier G., 2003, *PASP*, **115**, 763
- Chilingarian I. V., Zolotukhin I. Y., 2012, *MNRAS*, **419**, 1727
- Conselice C. J., 1999, *Ap&SS*, **269**, 585
- Cortese L., 2012, *A&A*, **543**, A132
- Cortese L., Catinella B., Boissier S., Boselli A., Heinis S., 2011, *MNRAS*, **415**, 1797
- Cortese L., et al., 2012, *A&A*, **544**, A101
- Cortese L., et al., 2014, *ApJL*, **795**, L37
- Courteau S., McDonald M., Widrow L. M., Holtzman J., 2007, *ApJL*, **655**, L21
- Croom S. M., et al., 2012, *MNRAS*, **421**, 872
- Dalcanton J. J., Spergel D. N., Summers F. J., 1997, *ApJ*, **482**, 659
- de Vaucouleurs G., 1959, *Handbuch der Physik*, **53**, 275
- de Vaucouleurs G., de Vaucouleurs A., Corwin Jr. H. G., Buta R. J., Paturel G., Fouque P., 1991, *Third Reference Catalogue of Bright Galaxies*
- Driver S. P., et al., 2011, *MNRAS*, **413**, 971
- Dutton A. A., van den Bosch F. C., Dekel A., 2010, *MNRAS*, **405**, 1690
- Emsellem E., et al., 2007, *MNRAS*, **379**, 401
- Emsellem E., et al., 2011, *MNRAS*, **414**, 888

- Faber S. M., Jackson R. E., 1976, *ApJ*, **204**, 668
- Falcón-Barroso J., Lyubenova M., van de Ven G., 2015, in Cappellari M., Courteau S., eds, IAU Symposium Vol. 311, IAU Symposium. pp 78–81 ([arXiv:1409.7786](#)), doi:10.1017/S1743921315003439
- Fall S. M., 1983, in Athanassoula E., ed., IAU Symposium Vol. 100, Internal Kinematics and Dynamics of Galaxies. pp 391–398
- Fall S. M., Efstathiou G., 1980, *MNRAS*, **193**, 189
- Fall S. M., Romanowsky A. J., 2013, *ApJL*, **769**, L26
- Fogarty L. M. R., et al., 2014, *MNRAS*, **443**, 485
- Fogarty L. M. R., et al., 2015, *MNRAS*, **454**, 2050
- Foster C., Arnold J. A., Forbes D. A., Pastorello N., Romanowsky A. J., Spitler L. R., Strader J., Brodie J. P., 2013, *MNRAS*, **435**, 3587
- Genel S., Fall S. M., Hernquist L., Vogelsberger M., Snyder G. F., Rodriguez-Gomez V., Sijacki D., Springel V., 2015, *ApJL*, **804**, L40
- Giovanelli R., Haynes M. P., Herter T., Vogt N. P., Wegner G., Salzer J. J., da Costa L. N., Freudling W., 1997, *AJ*, **113**, 22
- Goto T., Yamauchi C., Fujita Y., Okamura S., Sekiguchi M., Smail I., Bernardi M., Gomez P. L., 2003, *MNRAS*, **346**, 601
- Hernquist L., 1990, *ApJ*, **356**, 359
- Herschel W., 1786, Philosophical Transactions of the Royal Society of London Series I, **76**, 457
- Ho I.-T., et al., 2014, *MNRAS*, **444**, 3894
- Ho I.-T., et al., 2016a, *MNRAS*, **457**, 1257
- Ho I.-T., et al., 2016b, preprint, ([arXiv:1607.06561](#))
- Hubble E. P., 1926, *ApJ*, **64**, 321
- Hyde J. B., Bernardi M., 2009, *MNRAS*, **396**, 1171
- Jimmy Tran K.-V., Brough S., Gebhardt K., von der Linden A., Couch W. J., Sharp R., 2013, *ApJ*, **778**, 171
- Jorgensen I., Franx M., Kjaergaard P., 1996, *MNRAS*, **280**, 167
- Kelvin L. S., et al., 2012, *MNRAS*, **421**, 1007
- Kelvin L. S., et al., 2014, *MNRAS*, **439**, 1245
- Kormendy J., 1993, in Dejonghe H., Habing H. J., eds, IAU Symposium Vol. 153, Galactic Bulges. p. 209
- Kormendy J., Bender R., 2012, *ApJS*, **198**, 2
- Kormendy J., Kennicutt Jr. R. C., 2004, *ARA&A*, **42**, 603
- Krajinović D., et al., 2013, *MNRAS*, **432**, 1768
- Lange R., et al., 2015, *MNRAS*, **447**, 2603
- Lintott C. J., et al., 2008, *MNRAS*, **389**, 1179
- Lotz J. M., Primack J., Madau P., 2004, *AJ*, **128**, 163
- Markwardt C. B., 2009, in Bohlender D. A., Durand D., Dowler P., eds, Astronomical Society of the Pacific Conference Series Vol. 411, Astronomical Data Analysis Software and Systems XVIII. p. 251 ([arXiv:0902.2850](#))
- Mo H. J., Mao S., White S. D. M., 1998, *MNRAS*, **295**, 319
- Navarro J. F., Frenk C. S., White S. D. M., 1997, *ApJ*, **490**, 493
- Nilson P., 1973, Nova Acta Regiae Soc. Sci. Upsaliensis Ser. V, p. 0
- Obreschkow D., Glazebrook K., 2014, *ApJ*, **784**, 26
- Pedrosa S. E., Tissera P. B., 2015, *A&A*, **584**, A43
- Pracy M. B., et al., 2013, *MNRAS*, **432**, 3131
- Reynolds J. H., 1920, *MNRAS*, **80**, 746
- Robotham A. S. G., Obreschkow D., 2015, *Publ. Astron. Soc. Australia*, **32**, 33
- Romanowsky A. J., Fall S. M., 2012, *ApJS*, **203**, 17
- Rosse T. E. O., 1850, Philosophical Transactions of the Royal Society of London Series I, **140**, 499
- Sales L. V., Navarro J. F., Theuns T., Schaye J., White S. D. M., Frenk C. S., Crain R. A., Dalla Vecchia C., 2012, *MNRAS*, **423**, 1544
- Sánchez-Blázquez P., et al., 2006, *MNRAS*, **371**, 703
- Scannapieco C., White S. D. M., Springel V., Tissera P. B., 2009, *MNRAS*, **396**, 696
- Scodreggio M., Gavazzi G., Franzetti P., Boselli A., Zibetti S., Pierini D., 2002, *A&A*, **384**, 812
- Sharma S., Steinmetz M., Bland-Hawthorn J., 2012, *ApJ*, **750**, 107
- Sharp R., et al., 2006, in Society of Photo-Optical Instrumentation Engineers (SPIE) Conference Series. p. 0 ([arXiv:astro-ph/0606137](#)), doi:10.1117/12.671022
- Sharp R., et al., 2015, *MNRAS*, **446**, 1551
- Simons R. C., Kassim S. A., Weiner B. J., Heckman T. M., Lee J. C., Lotz J. M., Peth M., Tchernyshyov K., 2015, *MNRAS*, **452**, 986
- Snyder G. F., et al., 2015, *MNRAS*, **454**, 1886
- Spitzer Jr. L., Baade W., 1951, *ApJ*, **113**, 413
- Strateva I., et al., 2001, *AJ*, **122**, 1861
- Tapia T., et al., 2014, *A&A*, **565**, A31
- Taylor E. N., et al., 2011, *MNRAS*, **418**, 1587
- Teklu A. F., Remus R.-S., Dolag K., Beck A. M., Burkert A., Schmidt A. S., Schulze F., Steinborn L. K., 2015, *ApJ*, **812**, 29
- Toomre A., 1964, *ApJ*, **139**, 1217
- Tortora C., Napolitano N. R., Romanowsky A. J., Jetzer P., Cardone V. F., Capaccioli M., 2011, *MNRAS*, **418**, 1557
- Tully R. B., Fisher J. R., 1977, *A&A*, **54**, 661
- van den Bergh S., 1976, *ApJ*, **206**, 883
- Vulcani B., et al., 2014, *MNRAS*, **441**, 1340
- Walter F., Brinks E., de Blok W. J. G., Bigiel F., Kennicutt Jr. R. C., Thornley M. D., Leroy A., 2008, *AJ*, **136**, 2563
- Weijmans A.-M., et al., 2014, *MNRAS*, **444**, 3340
- Wheeler C., Pace A. B., Bullock J. S., Boylan-Kolchin M., Onorbe J., Fitts A., Hopkins P. F., Keres D., 2015, preprint, ([arXiv:1511.01095](#))
- Wu X., Gerhard O., Naab T., Oser L., Martinez-Valpuesta I., Hilz M., Churazov E., Lyskova N., 2014, *MNRAS*, **438**, 2701
- York D. G., et al., 2000, *AJ*, **120**, 1579
- Zavala J., Okamoto T., Frenk C. S., 2008, *MNRAS*, **387**, 364
- Zavala J., et al., 2015, preprint, ([arXiv:1512.02636](#))
- Zibetti S., Charlot S., Rix H., 2009, *MNRAS*, **400**, 1181